Microscopy and Microanalysis, 2023, **29**, 1566–1578
https://doi.org/10.1093/micmic/ozad087
Advance access publication 28 August 2023
Original Article

Microscopy AND Microanalysis

Structural Identification and Observation of Dose Rate–Dependent Beam-Induced Structural Changes of Micro- and Nanoplastic Particles by Pair Distribution Function Analysis in the Transmission Electron Microscope (ePDF)

Christian Rohner[1,*], Christoph Pratsch[2], Robert Schlögl[1,3], and Thomas Lunkenbein[1,*]

[1]*Department of Inorganic Chemistry, Fritz Haber Institute of the Max Planck Society, Faradayweg 4-6, 14195 Berlin, Germany*
[2]*Helmholtz-Zentrum Berlin für Materialien und Energie GmbH, Department X-Ray Microscopy, Hahn-Meitner-Platz 1, 14109 Berlin, Germany*
[3]*Department of Heterogeneous Reactions, Max Planck Institute for Chemical Energy Conversion, Stiftstraße 34-36, 45470 Mülheim an der Ruhr, Germany*

***Corresponding author:** Christian Rohner, E-mail: crohner@fhi-berlin.mpg.de, Thomas Lunkenbein, E-mail: lunkenbein@fhi-berlin.mpg.de

Abstract

Micro- and nanoplastics (MNPs) are considered a possible threat to microorganisms in the aquatic environment. Here, we show that total scattering intensity analysis of electron diffraction (ED) data measured by transmission electron microscopy, which yields the electron pair distribution function (ePDF), is a feasible method for the characterization and identification of MNPs down to 100 nm. To demonstrate the applicability, cryo ball–milled powders of the most common polymers [i.e., polyethylene , polypropylene, polyethylene terephthalate, and polyamide] and nano-sized polystyrene and silica spheres were used as model systems. The comparison of the experimentally determined reduced pair density functions (RDFs) with model RDFs derived from crystallographic data of the respective polymers allows the distinction of the different types of polymers. Furthermore, carbon-based polymers are highly beam-sensitive materials. The degradation of the samples under the electron beam was analyzed by conducting time-resolved ED measurements. Changes in the material can be visualized by the RDF analysis of the time-series of ED patterns, and information about the materials in question can be gained by this beam damage analysis. Prospectively, ePDF analytics will help to understand and study more precisely the input of MNPs into the environment.

Introduction

Micro- and nanoplastics (MNPs) are ubiquitously found in all parts of the environment (Ng et al., 2018). They are considered a possible threat especially to microorganisms in the aquatic environment (Alimi et al., 2018). However, a meaningful quantification of MNP pollution in the world's water has yet to be achieved (Mintenig et al., 2018). To date, there is no standard procedure for the determination of the microplastic content of samples taken from the environment (Mintenig et al., 2018). Instead, a number of thermogravimetric or infrared (IR) and Raman microscopic methods are being examined for application (Dümichen et al., 2017; Paul et al., 2019; Goedecke et al., 2020; Primpke et al., 2020; Wander et al., 2020). While most toxic effects are reported on MNPs with sizes $< 10\ \mu$m, especially, a quantification of this size class is lacking (Kögel et al., 2020). A critical review of concurrent methods focused on MNP content determination in fresh water and drinking water was given in 2019 highlighting the importance of the development of new analytical methods for the characterization of small MNPs (Koelmans et al., 2019).

In general, this size boundary originates from technological and physical constraints of the methods. For instance, the solid material in a sample of sea or fresh water is separated from the liquid by cascade filtration. As the smallest pore diameter of suitable commercial filters are around $5\ \mu$m, the smallest size fraction left in the filtrate contains all particles of sizes $< 5\ \mu$m. A further separation into smaller size fractions by techniques such as magnetic field flow fractionation, gel electrophoresis, and size-exclusion chromatography is discussed but might require improvements of the separation efficiency before a reliable application to nanoplastic separation is feasible (Nguyen et al., 2019). Mass spectrometry can usually determine the mass fractions of different types of plastics in a sample precisely, but a special difficulty exists for markers of polyethylene (PE) which cannot be distinguished from those of fatty acids. Therefore, only an upper limit of the PE mass content can be determined (Goedecke et al., 2020).

Optical Raman/IR microscopy offers an alternative way to investigate microplastics (Wander et al., 2020). The improvement of optical Raman/IR microspectroscopy has only recently lowered the detection limit to particles with a diameter of $0.5\ \mu$m (Faull et al., 2021). Due to the diffraction limit of optical light sources, smaller particles cannot be distinguished if they are in close proximity to each other and reliable information on their sizes cannot be obtained.

However, we show here that pair distribution function analysis of electron diffraction (ED) data acquired by transmission electron microscopy [TEM, electron pair distribution function (ePDF)] can be used for the polymer-specific

Received: March 31, 2022. **Revised:** July 22, 2022. **Accepted:** August 2, 2023

identification of microplastics and nanoplastics in the size regime of a few micrometers down to <100 nm spatial resolution, decreasing the detection limit by a factor of 5.

In brief, PDFs can be understood as a histogram of the distances between atoms in a material (Proffen et al., 2003). They can be extracted by inverse Fourier sine transformation (FT) of properly corrected and normalized total X-ray (Chupas et al., 2009), neutron (Culbertson et al., 2020), or electron scattering intensity (Hoque et al., 2019). The reduced pair distribution function (RDF), $G(r)$, is the direct result of this treatment of the data. This function is also known as the differential radial distribution function (DRDF; Wang & Yeh, 1981). The RDF displays the short- and medium-range order of amorphous and semicrystalline materials. While for crystalline materials, this information is more easily available via Bragg reflection analysis, for semicrystalline or amorphous materials, Bragg reflections are weak or completely absent (Petkov et al., 2013). A value of zero in the RDF represents the average density of a material described by the number of atoms per unit volume. Positive and negative values represent a higher and lower density, respectively, at a given distance r measured from a randomly chosen atom. For a multi-elemental material, the overall RDF is the weighted sum of the individual RDFs taken over all element combinations. The weighting factors are determined by the individual atomic scattering factors. A comprehensive description of the method can be found in the literature (Takeshi & Billinge, 2012; Mu et al., 2013; Gorelik et al., 2019).

The technique has been widely applied to the structural characterization of metal nanoparticles (Hoque et al., 2019), defect structures (Chanakian et al., 2020), metallic glasses (Sheng et al., 2006), functional materials (Willinger et al., 2017), and organic materials (Gorelik et al., 2015).

In the analogous form of radial distribution function analysis, it has been extensively used for the determination of free molecular structures using gas-phase ED (GED) since the mid-1950s (Hilderbrandt & Bonham, 1971). While for many applications and materials in TEM, hydrogen atoms often remain elusive, the structural parameters (i.e., bond lengths and angles and vibrational displacement factors) including C–H bond length of organic compounds ranging from *n*-alkanes (e.g., pentane, hexane, and heptane) to larger complexes such as octa(*m*-trifluoromethylphenyl)porphyrazine determined by GED are reported (Bonham et al., 1959; Zhabanov et al., 2015). It was recently shown that the ePDF technique can be used in combination with 4D-scanning TEM datasets to gain local structural information of amorphous materials with spatial resolution on the nanoscale (Mu et al., 2016, 2019; Wang et al., 2021).

To assess the applicability of the ePDF method to the problem of MNPs, we examined a set of artificially comminuted samples of the most common commercial organic polymers (Geyer et al., 2017), i.e., PE, polypropylene (PP), polyethylene terephthalate (PET), polystyrene (PS), and polyamide (PA). RDFs or DRDFs of these materials obtained by methods other than ED, e.g., X-ray or neutron diffraction, are reported for PE (Gupta & Yeh, 1979; Narten, 1989; Laridjani & Leboucher, 2009), PP (Marigo et al., 1991; Abu-Sharkh, 2004), PET (Gupta & Yeh, 1978; Neissendorfer, 1982; Golmohammadi et al., 2020), PA (Terban et al., 2020), and PS (Wecker et al., 1972; Kobryn et al., 2014).

Carbon-based polymers are known to be among the most electron beam–sensitive materials (Kumar & Adams, 1990). Recently, Kisielowski et al. have proposed and experimentally verified a different model of electron scattering that treats all electron scattering as coherent but inelastic (Kisielowski et al., 2021, 2022). The consequence of this treatment is that beam damage is dependent not only on the total dose and acceleration voltage but also on the dose rate and on the area illuminated by the beam. The critical dose, D_c, can be altered by the experimental conditions applied in the diffraction measurements. It is shown that radiation hardness correlates very well with heat capacity and heat conductivity, i.e., melting of a sample can be a dominant beam damage mechanism for radiation soft matter. This does not stand in contrast to the "traditional" understanding, which assumes radiolysis of bonds to be the primary beam damage mechanism, but it explains how certain conditions [e.g., cryogenic (cryo)TEM] applied to certain material classes influence D_c. In our study, we conducted two sets of measurements at different dose rates and illuminating two different areas. In effect, our experimental conditions are roughly comparable to the experimental conditions of Kisielowski et al. and we refer to ours as "The Molecular Foundry (TMF)-like" and "Dow-like" in analogy to their original article (see "TEM" section for the details). As we will show, our RDF results can be interpreted to confirm and slightly enhance the experimental conditions of Kisielowski et al. in showing distinct beam damage mechanisms, which are predominantly caused by heating of the samples at a low dose rate/small illuminated area and heating and radiolysis at a moderate dose rate/large illuminated area.

To our knowledge, the presented study is the first to systematically measure C–H pair distance peaks using the ePDF method on carbon-based polymers. A distinction between PET and either PE, PP, or PA is shown to be very clear in the RDF plots, while a distinction among PE, PP, and PA can only be made from differences in intensities in regions of the PDF where intensities are most affected by fitting errors caused by multiple scattering (thickness) effects. Yet, pending a systematic verification excluding thickness variations between the examined materials, based on the agreement of calculated model RDFs and our experimental results, the ePDF method could be sufficient for a distinction of the latter three polymers as well.

Materials and Methods

Materials

PE, PP, PA, and PET MNPs were prepared using industrial pellets (1–3 mm) kindly provided by plastic manufacturers with the support of Plastics Europe Deutschland e.V. and cryo ball milled as previously described (Paul et al., 2019).

Powder samples were prepared for TEM measurement dry or by drop casting of isopropanol (Roth, Rotisolv, and HPLC grade) suspensions on continuous carbon-coated Cu grids (Plano, 200 mesh).

One hundred-nanometer PS spheres were purchased from BS-particles (Prod.-No. HS0010-20). One hundred-nanometer amorphous SiO_2 spheres were purchased from Sigma-Aldrich.

TEM

TEM was conducted on a double Cs–corrected JEOL ARM200F equipped with a 2k × 2k Gatan Orius SC200D and a 4k × 4k Gatan OneView camera at an emission current of 1 μA and a Cs-corrected Titan 80–300 equipped with a 4k × 4k TVIPS XF416R. The acceleration voltage was set to

200 kV, and a 70-μm C2 aperture was used on both TEMs. Images were recorded using Gatan DigitalMicrograph and TVIPS EM Menu. Sequential diffraction images (serial ED) were recorded on the respective cameras at a frame rate of 1–3.3 fps using the TemRecorder plugin for GMS or the series acquisition tool in EM Menu where a delay was set to 500 ms between acquisitions. For "TMF-like" conditions, the illumination on the JEOL was spread to 2 μm and the selected area was 1.75 μm in diameter by inserting a 40-μm SA aperture. The dose rate was approximately $d_r \cong 0.45$ e Å^{-2} s^{-1}. For "Dow-like" conditions, on the Titan, the illumination was 12 μm in diameter, the selected area was 0.65 μm using a 40-μm aperture, and the dose rate was approximately $d_r \cong 1.6$ e Å^{-2} s^{-1}.

The camera length was adjusted to reach a scattering vector of at least $Q > 20$ Å^{-1}. Lens settings for optimal diffraction were determined on an AuPd calibration sample and finely adjusted on amorphous carbon regions for each sample. ED patterns of amorphous carbon were measured for background subtraction.

Areas of interest were located in low magnification (<5,000x) mode with a widespread beam in order to minimize the beam dose prior to the ED measurements. Subsequently, the beam was blanked and the lens settings for optimal diffraction were loaded. The ED acquisition series was started at the exposure of the sample to the parallel electron beam. Selected area ED (SAED) was used for cryo ball–milled microparticles, and nanobeam diffraction was used for nanoparticles.

Data Reduction

All image manipulations were performed using ImageJ. All ED patterns of a time series were first binned to a resolution of 512 × 512 (Orius) or 1,024 × 1,024 (TVIPS). Then, the images were temporally averaged over a number of frames, such that the total exposure time was virtually set to ~3 s per frame. The series were filtered to remove shot noise by applying a Kalman filter in reverse, i.e., from the last frame to the first. The last five frames were disregarded in the later analysis. Lastly, outliers were removed. The same procedure was applied to a series of ED patterns collected on the clean continuous amorphous carbon support film for subsequent background subtraction.

Determination of RDFs

All calculations were performed using MATLAB. The method involves the simultaneous determination of the RDF from an experiment and a trial model. Fit parameters, data range, additional data treatments, and trial models were iteratively adjusted until a good qualitative agreement between model and experimental RDF was found. The parameters are further explained in section "Extraction of RDFs from the Experiment."

Modeling of RDFs

Model RDFs were calculated by using a "forward and reverse" approach (Fig. 1). Forward, from a given set of 3D atom coordinates of a model molecule or section of a crystal structure (Fig. 1a), a histogram of atom–atom pair distances can be calculated (Fig. 1b). The radial scattered intensity (which is the powder diffraction pattern), $I(Q)$ (Fig. 1c), is then calculated from Debye's equation [equation (1)] for scattering of isotropic media using the atom–atom pair distances (Debye, 1915).

$$I(Q) = N*\langle f(Q)^2\rangle + \sum_{j\neq k}^{N} f_j(Q) f_k(Q) \frac{\sin(Qr_{jk})}{Qr_{jk}}. \qquad (1)$$

The equation takes the assumption that infinite copies of a 3D set of atoms in a model exist and take up all possible orientations in space, i.e., form a powder. N is the total number of atoms in the model. $f(Q)$ are the atomic scattering factors,

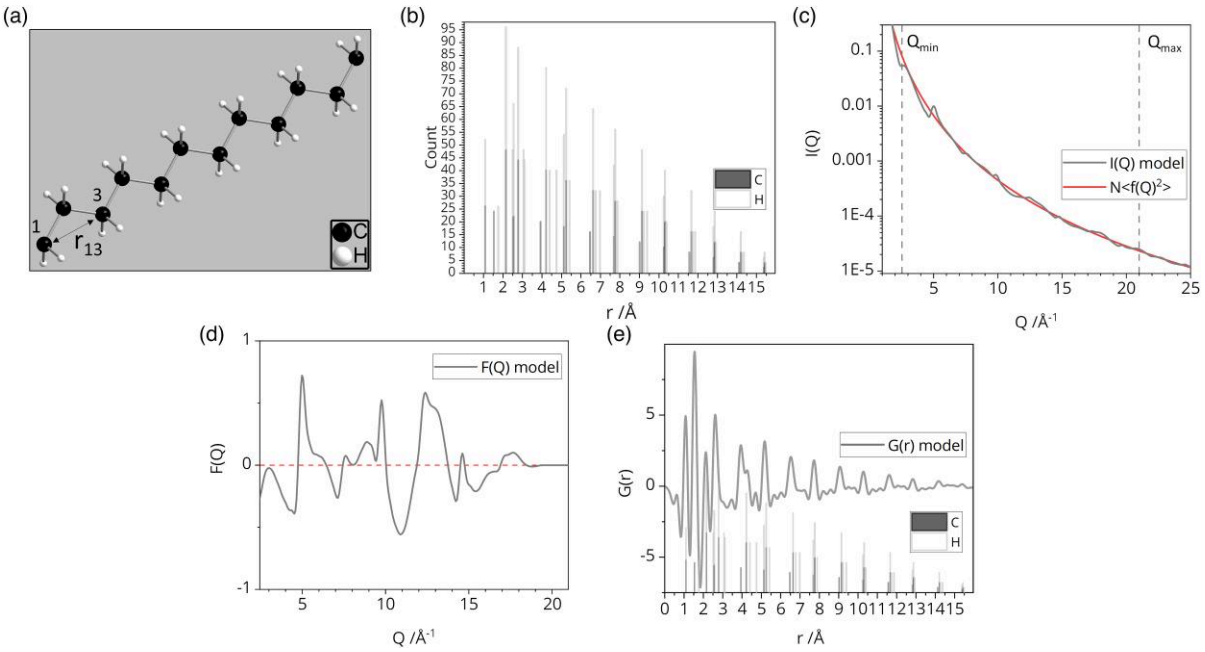

Fig. 1. Model RDF calculation. (**a**) Structural model with 3D coordinates. The arrow indicates the distance r_{13} between arbitrarily chosen atoms 1 and 3. (**b**) Histogram of all distances measured from each atom to all others. For $N = 36$ atoms, these total to $N*(N-1) = 1{,}260$ pair distances, where the element color is plotted for the atoms j. (**c**) Radial scattered intensity, $I(Q)$ model, calculated based on the pair distances in (**b**), according to equation (1). The single-atom scattering ($N < f(Q)^2 >$) is shown in red. (**d**) The structure function, $F(Q)$, calculated by equation (4). (**e**) The reduced pair distribution function, $G(r)$ [equation (2)], and r_{jk}.

which were calculated for each element using the parametrized form provided by Lobato and Van Dyck (2014). The angled brackets "$\langle f(Q)^2 \rangle$" denote a compositional average which was calculated using the stoichiometry of the model. Q is the magnitude of the momentum transfer vector defined by $Q = (4\pi \sin\theta)/\lambda$ with the scattering angle being 2θ and the electron wavelength λ. The indices j and k denote the individual atoms, and r_{jk} is the separation between atom j and atom k. r_{jk} contain the structural information, which is now reduced from 3D to 1D information.

The reverse approach retrieves the r_{jk} values from the radial intensity by inverse Fourier transformation of the reduced structure function $F(Q)$ according to equations (2) and (3) (Fig. 1d):

$$G(r) = \frac{2}{\pi} \int_{Q_{\min}}^{Q_{\max}} F(Q) \sin(Qr) dQ \,, \tag{2}$$

$$F(Q) = Q \frac{I(Q) - N\langle f(Q)^2 \rangle}{N\langle f(Q)^2 \rangle}. \tag{3}$$

$G(r)$ is the RDF. The reduced structure function, $F(Q)$, reflects equation (1) resolved to the sum of sinc functions, normalized to the number of atoms and the squared ensemble average of the single-atom scattering factors. For a multi-elemental material, the latter is an approximation, because $f_j(Q)f_k(Q)$ can be from different elements and the factors are convolved with the pair distances r_{jk}. A deconvolution cannot be achieved from a single experimental measurement. For our analysis, this inaccuracy can be neglected, as we introduce this error in the model calculation in the same way that it occurs in the analysis of the experimental data. In consequence, the error will be the same in both calculations, if the stoichiometry of the model is chosen carefully enough.

All model structures employed in this analysis were based on crystallographic data (Kavesh & Schultz, 1970; Simon & Argay, 1978; Huan et al., 2016). Suitable sections of the crystal structure of a candidate material were chosen based on an initial analysis of the experimental data. For instance, if the experimental RDF showed no long-range order or if interchain pair distances were found to be absent, the size of the model was reduced to single chains of only a few monomer length.

Extraction of RDFs from the Experiment

After careful determination of the center of the pattern, the intensities of the processed ED series were azimuthally averaged and an additional interpolation step was used to suppress artifacts from the pixels of the detector, yielding the experimental radial intensity profile $I_{\exp}(Q)$ of each frame in the stack. To calculate the experimental reduced structure function $F_{\exp}(Q)$, equation (3) was used with the following modifications. First, $\langle f(Q)^2 \rangle$ was calculated from the nominal stoichiometry of the material under examination, and then, $N\langle f(Q)^2 \rangle + C$ was fitted to $I_{\exp}(Q)$ by adjusting N and C, where C is a constant background. As $I_{\exp}(Q)$ contains contributions from inelastic and incoherent as well as multiple scattering, a perfect fit cannot be achieved for all Q. In order to isolate the coherent scattering, a pseudomultiple scattering correction was achieved by fitting an nth-order polynomial $P^n(Q)$ to $F_{\exp}(Q)$. The polynomial was then subtracted from the experimental result before the $\mathrm{RDF}_{\exp}$ was calculated [see also equation (4)]. This results in the removal of often very large peaks in the unphysical region of the RDF, $G(r)$, at $0\ \text{Å} < r < 1\ \text{Å}$, the correction of peak intensities in the small r region ($1 < r < 2$ Å) and the removal of weak oscillations stretched out over long ranges of the RDF (Mu et al., 2013).

By applying a moving average filter, M, to the reduced structure function, residual noise at high Q was removed. Last, a cosine damping function, $D(Q)$, was multiplied to the high angle range of the structure function to suppress high-frequency oscillations in the RDF that are due to the finite range of the signal (Fourier truncation error). The full treatment is represented in equation (4).

$$F(Q) = M\left(Q \frac{I(Q) - \left(N\langle f(Q)^2 \rangle + C\right)}{N\langle f(Q) \rangle^2} - P^n(Q) \right) * D(Q) \,. \tag{4}$$

The $G(r)$ were then determined by inverse Fourier sine transform of the normalized and corrected $F(Q)$ with the integration boundaries set to a suitable window of angles, according to equation (2). The low angle boundary, $Q_{\min}$, was set at $Q_{\min} = 2.51\ \text{Å}^{-1}$ to exclude small angle scattering and effects of the direct beam. The high angle boundary, $Q_{\max}$, was set depending on the signal-to-noise-ratio of the individual measurement series.

Apart from polynomial fit subtraction and moving average filtration, the same treatment was performed on the calculated powder diffraction pattern of the model structure. The Fourier transform was applied over the same range of Q and with the same angular resolution. This parallel calculation permits direct comparison between the model and the experiment for the structure function and the RDF. If a suitable model was chosen, it allows identifying artifacts introduced by the Fourier transform (i.e., small ripples in regions between peaks; Fig. 1e) and correcting the fit factor N and the baseline factor C. The fit factors N and C were then iteratively adjusted for the first frame of a series, so that the intensity maximum of the first C–C bond peak in the model $G(r)$ and the experimental $G(r)$ was equal. This resulted in a good fit of $N\langle f(Q)^2 \rangle + C$ to $I_{\exp}(Q)$ at high Q, but an underestimation of $I_{\exp}(Q)$ by $N\langle f(Q)^2 \rangle$ at intermediate Q, and an overestimation at small Q. The difference was subtracted by the polynomial fit as shown in Supplementary Figure 1. For all subsequent frames, the factor N was scaled by the integrated intensity of $I_{\exp}(Q)$ in each individual frame. The lower integration limit for this was set to $Q_{\min} = 2.51\ \text{Å}^{-1}$.

Results

Cryo ball–milled PE, PP, PET, and PA powders were examined in the TEM. The samples are white powders of polydisperse particles with sizes between ~5 and 200 μm. Representative TEM images are included in the overview figure of each sample, which are presented in the Supplementary Figures 2–9. The particles are irregularly shaped and often exhibit jagged edges or flaps on the edges, which leads to a broad range of sample thickness in different regions. The diffraction data underlying the presented RDFs were recorded on thin edge regions of the particles (Supplementary Figs. 2e–9e and 11e).

PE TMF-Like Conditions

Figure 2 illustrates the consecutive steps of the analysis demonstrated on the example of a thin region of the cryo ball–

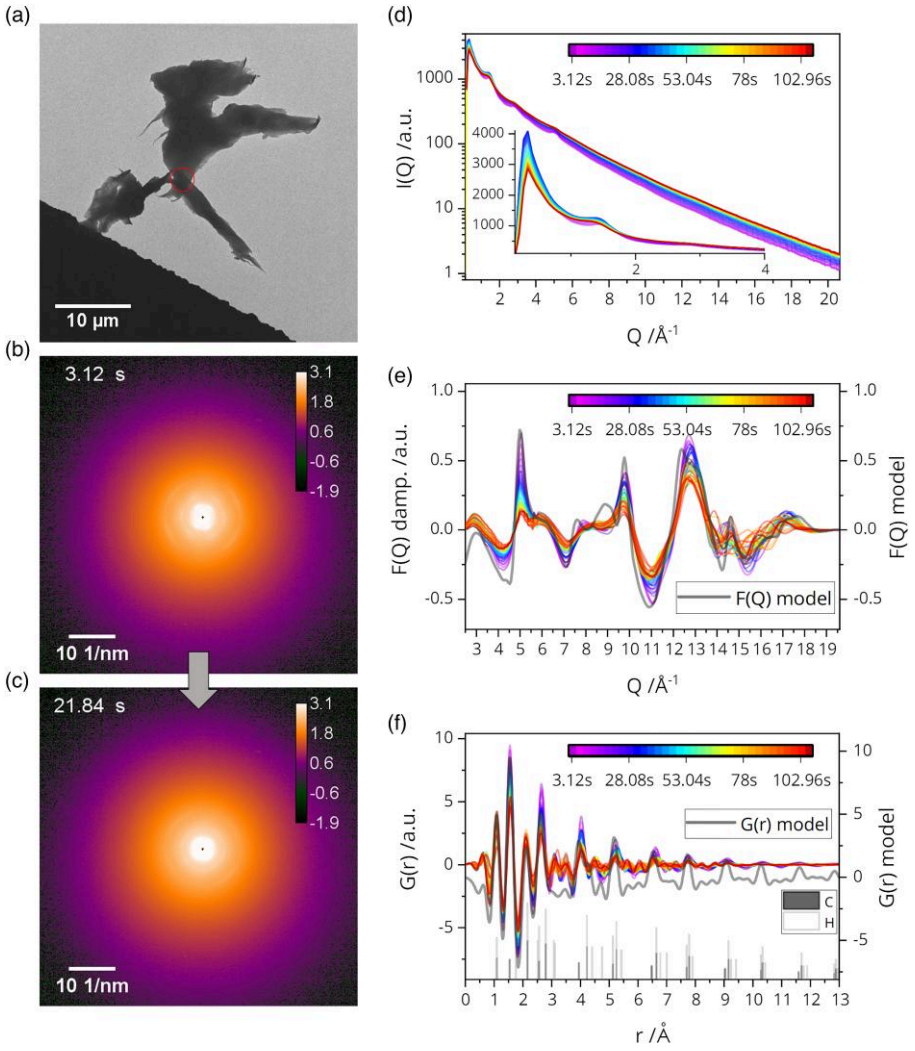

Fig. 2. TEM characterization and analysis of the ED time series measured on a cryo ball–milled PE particle. (**a**) TEM image of a PE particle with the approximate position of the selected area aperture indicated by the red circle. (**b**) The first frame of the ED series shown with intensity on a logarithmic scale. The full series is available in Supplementary Video 1. (**c**) The seventh frame of the ED series. (**d**) Annular average intensity, $I(Q)$, plotted over the full measured range on a logarithmic scale (with inset showing the small angle region on linear scale). (**e**) The corrected and damped structure function $F(Q)$, calculated from A and plotted over the range in Q, that was Fourier transformed to gain the RDFs, $G(r)$ plotted in (**f**). The gray curves in (**e**) and (**f**) are the corresponding simulated $F(Q)$ and $G(r)$, respectively, calculated from the model shown in (**b**). The color scale bars in (**d–f**) indicate the measurement time of the ED time series. Each $I(Q)$ was calculated from an average ED pattern taken over six frames of 0.52 s exposure per frame (the odd number comes from a delay due to readout and writing, and the exposure time was set to 0.5 s).

milled PE. Serial ED patterns (time series/dose series) were recorded from the region which is highlighted by the red circle in Figure 2a. The first frame of the ED series is shown in Figure 2b, where distinct reflections and quarter rings are visible. This indicates a relatively high crystallinity of PE prior to the exposure to the electron beam. This ED pattern shows the highest degree of order that has been found for all polymers within this study (compare an alternate measurement of PE in Supplementary Fig. 13 and Video 9). The four innermost, brightest reflections can be assigned to {110} lattice planes with a d-spacing of $d = 4.1$ Å [Fig. 2b, (space group $Pna2_1$) (Kavesh & Schultz, 1970)]. All other reflections are strongly broadened or absent [e.g., (200)]. All measured ED series show a rather quick evolution under beam exposure, and any relevant texture or significant crystallinity vanishes at some point (Supplementary Videos 1–9). For PE, this was the case after ≅15–20 s of exposure and is shown in Figure 2c. The calculated dose at this time of exposure is 7–9 e Å^{-2}, which is on the order of reported values for the critical dose of PE (Reimer, 1984; Kumar & Adams, 1990). The full ED series can be found in Supplementary Video 1.

The logarithmic plot of the radially integrated $I(Q)$ is mostly featureless apart from three broad reflections in the first few graphs of the time series (Fig. 2d, purple). An increase in total scattering intensity with increasing exposure time can be observed (Fig. 2d, purple, yellow, and red curves), at which the three reflections broaden and disappear. This is reflected in the plot of the fit factor, N, against the acquisition time (Supplementary Fig. 2f). Apparently, while the crystallinity of the polymer decreases, the amount of material under the SA increases, which could be explained by a simultaneous condensation of low-density amorphous regions, disruption of crystalline order, and a drift of the sample under the beam. The reduced structure functions, $F(Q)$, (Fig. 2e) demonstrate the loss in order with increased beam

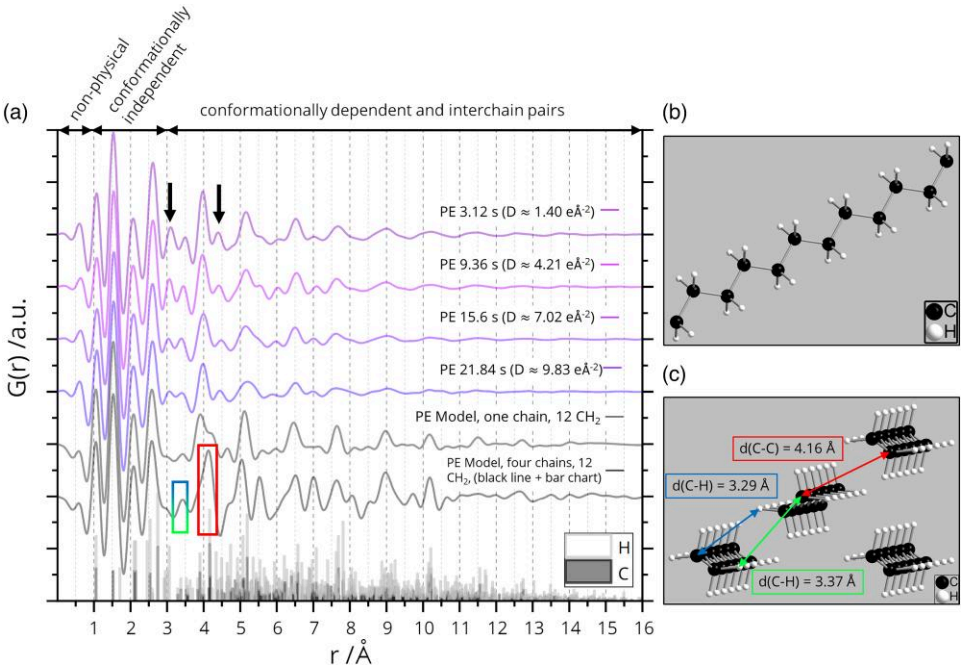

Fig. 3. (**a**) RDFs calculated for the first (3.12 s), third (9.36 s), fifth (15.6 s), and seventh (21.84 s) frames of the PE ED series together with model RDFs, one 12 CH2-unit long chain (gray, structural model in (**b**)) and four 12 CH2-unit long chains (black, structural model in (**c**)), and the histogram of r_{jk} of the model. The model was based on crystallographic data (Kavesh & Schultz, 1970). The double arrows at the top of (**a**) indicate distance ranges where peaks are nonphysical (<0.9 Å), conformationally independent for most aliphatic polymers (0.9–3 Å), and conformationally dependent with interchain pair distance peaks potentially appearing, in addition (>3 Å). The blue, red, and green boxes in (**a**) indicate the distances between interchain C–H and C–C pairs, as shown in (**c**) by the colored double arrows. The black arrows in (**a**) indicate the C–C third and fourth neighbor pair distances of 3.1 and 4.5 Å, respectively, that occur when a PE chain adopts the gauche conformation.

dose which is indicated by a decrease of the sharpness of the peaks. A comparison of the simulated $F(Q)$ model (Fig. 2e, gray curve) and the experimental $F(Q)$ displays a good agreement at short exposure to the electron beam (Fig. 2e, purple curves). The corresponding RDFs, calculated from each structure function $F(Q)$ of the time series and from the model $F(Q)$, are shown in Figure 2f (colored graphs and gray graph, respectively) together with the histogram of the r_{jk} employed in the calculation of the model RDF [i.e., $I(Q)$ model calculated by equation (1); Fig. 1c]. For a better comparison, selected RDFs have been stacked and are presented in Figure 3a.

For PE, the selected model is a straight chain of twelve CH_2 units (Fig. 3b), which is a section of its crystal structure (space group: $Pna2_1$; Kavesh & Schultz, 1970). Tabulated values for the short-range pair distances calculated from the model can be found in Supplementary Table 1. It was found as a good match after the size of the section of the crystal structure was iteratively decreased from multiple unit cells to the single chain until all but two small peaks (between 3 and 3.5 Å) were accounted for and no additional peaks could be revealed within the simulated $G(r)$. As ePDFs seem to generally show a decay of the peak intensities proportional to r (Gorelik et al., 2019), it can be estimated from the peak intensity at 11.5 Å that straight regions of the polymer chains exist which are at least nine CH_2 units long.

Figure 3 displays a comparison of the RDF calculated from the first, third, fifth, and seventh frame of the ED series, the single-chain model RDF, and a more crystalline model RDF consisting of sections of four next neighbor parallel chains in the same crystal structure. While during the exposure to the beam for up to ~21.84 s, i.e., an accumulated dose of

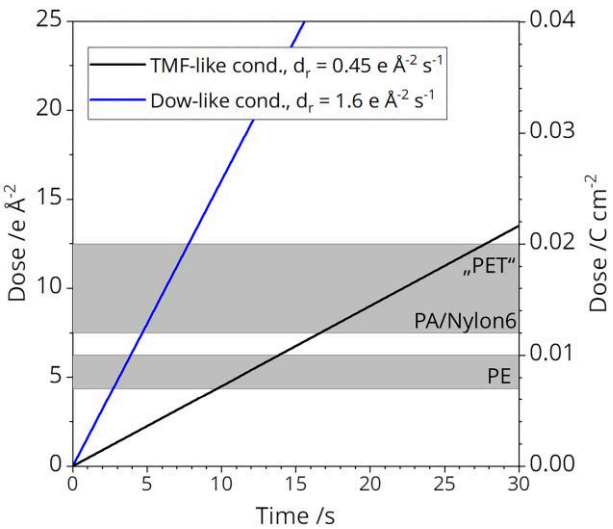

Fig. 4. Accumulated dose versus exposure time for the two different beam condition experiments. The critical dose for the disappearance of all ED features for PE (0.7–1.2 10^{-2} Ccm^{-2} @100 kV) and PA/Nylon6 (1.2–2 10^{-2} Ccm^{-2} @100 kV) or mass loss for polyester ("PET," 2×10^{-2} Ccm^{-2} @75 kV), respectively, are shown as gray areas. The values were taken from (Reimer, 1984; Kumar & Adams, 1990).

$D \cong 9.83$ e Å^{-2}, all texture disappears from the ED patterns (Figs. 2b, 2c). Furthermore, the RDFs do not show any peak shifts or changes in relative intensities, but their overall intensity decreases (see Fig. 4 for a plot of the accumulated dose versus exposure time together with literature values for the known critical doses of the polymers). Peaks at large r are

vanishing first. The two peaks in the region of $r \approx 3.1$–3.5 Å are not accounted for by the model. The peaks at $r = 3.1$ Å and $r = 4.5$ Å (marked by black arrows in Fig. 3a) can be attributed to third and fourth neighbor distances, respectively, when the dihedral angle between four carbon atoms is 60°, suggesting local gauche rotational conformation of the PE chains (Supplementary Fig. 10). The peak at $r = 3.5$ Å could be assigned to interchain contacts spanning from a carbon atom to a hydrogen atom of a neighboring chain (Fig. 3c). Yet, additional peaks that correspond to different interchain distances are absent in the RDF (Fig. 3a, black line, and Fig. 3c) four-chain model, e.g., the red marked distances. In addition to the four-chain model, several different model structures have been calculated starting from 25 chains, each of them composed of 12 monomers, down to only one chain with a length of monomers. The results are presented in Supplementary Figure 11. This indicates that on average, *anti*-conformation segments of the polymer are about 9–12 CH_2 units long. Because no significant interchain peaks are present in the RDF, it can be concluded that while the chains may be parallel over short distances (giving texture to the ED), they are randomly shifted with respect to each other along the chain direction, rotated around the chain direction, or disordered by curvature (Kübel et al., 2000).

The decay in peak area in the RDF with extended beam exposure (Fig. 3a, colored curves) could be attributed to the decrease of intrachain order. On one hand, a possible explanation for this is that any radiolysis of C–C bonds in PE leads to a chain scission. The higher mobility of shorter chains could subsequently lead to a relaxation of stress that is stored in the material, and long-range order is diminished. On the other hand, as electrons interact strongly with matter, a broad range of interactions spanning from phonon and plasmon excitation, excitation of bond vibrations, core electron ejection to displacement of atoms (knock-on damage), and associated energy dispersion paths could also lead to a displacement of polymer chains away from more ordered configurations. A decrease of the RDF peak area is also found in the simulation series presented in Supplementary Figure 12. Additionally, the material seems to consolidate. This is corroborated by the observed increase in the integrated scattered intensity (Fig. 2d) and, hence, the fit factor N (Supplementary Fig. 2g). Note, if N is increased in a calculation, the intensities in the PDF will also decrease. Therefore, the calculation was repeated with a constant N value, which still resulted in a decrease of the intensities in the PDF. It was, thus, found that the presented fitting procedure, i.e., using the integrated intensity to scale N, has an advantage over the usual least squares fitting of $N\langle f(Q)^2\rangle + C$ to $I(Q)$. The change of the intensities in the RDFs between sequential frames is smoother compared with that in the established least square fitting, as the least square fit can be more easily disturbed by random noise.

At the low dose level, even during long beam exposure, a significant shift of peaks which can be attributed to directly bonded or second neighbor atoms is absent. The proposed degradation mechanism of polymers by radiolysis of C–C bonds or other electron–matter interactions under a low dose rate ($\cong 4.5$ e Å^{-2} s^{-1}) results in a less ordered PE, while the carbon–hydrogen bonds remain almost unaffected. The latter is evident by comparison of the intensities of the two C–H-pair peaks at $r = 1.1$ Å and $r = 2.2$ Å, which are almost constant for all frames of the RDF series.

Comparison with PP, PET, and PA (TMF-Like Conditions)

A comparison of the RDFs of PE, PP, PET, and PA, measured under low dose rates are presented in Figure 5 accompanied by their respective structural models. Tabulated values for the short-range pair distances calculated from the models for PP, PET, and PA can be found in the Supplementary Tables 2–4. The full ED series underlying the RDFs are given in the Supplementary Videos 2–4. Overall, a good qualitative fit between the experimental and simulated RDF was achieved for each first frame of a time series (Fig. 5a). Clear and characteristic differences are visible between the respective RDFs of the four materials in peak positions, peak intensities, and peak evolution under continued exposure to the electron beam.

The discussion on PE can be extended to the case of PP. Here, a single-chain section of an isotactic PP was chosen as the model (Huan et al., 2016). The carbon chain contains 12 carbon atoms with six methyl side groups (Fig. 5b). Model and experimental RDFs agree reasonably well (Fig. 5a).

Interestingly, for PP, the peaks at 1.1 and 1.55 Å which can be assigned to C–H and C–C bond lengths, respectively, are broadened and are more strongly overlapping in the experimental PP-RDF (measured with $Q_{max} = 21.2$ Å^{-1}) than in the simulation or in the experimental PE-RDF (measured with $Q_{max} = 19.6$ Å^{-1}). The broadening is also found for the second neighbor C–H and C–C pair distances at 2.2 and 2.6 Å. This finding was unexpected but also appears in the "Dow-like" experiments (see Fig. 6 below). While we cannot fully exclude a measurement artifact at this point, a possible explanation could lie in the presence of primary, secondary, and tertiary C–H bonds and the methyl group in PP (Fig. 5b, PP). The model does include slightly different bond lengths between them (compare Supplementary Table 2), but the extent of the peak broadening in the experiment cannot be explained by differing bond lengths alone. Rather, it could be due to the more complex vibrational properties of the C–H bonds in PP compared with PE.

With extended beam exposure, the peak area of PP-RDF decreases indicating a loss in structural order (Fig. 5a, PP). For PP, the loss of structural order is not as pronounced as for PE, which can be caused by the following: (1) not every C–C bond radiolysis event leads to a scission of a chain because methyl side groups could be cleaved off and (2) a lower degree of crystallinity of PP compared with PE prior to the experiment.

For PET and PA, a different position of the principal peak of the RDF is observed (Fig. 5a, PET and PA) compared with PE and PP. It is centered on shorter distances, r, compared to PP/PE in all frames of the series (dashed line in Fig. 5a). This can be attributed to the presence of heteroatoms in PET (i.e., oxygen) and PA (i.e., nitrogen and oxygen). C–O and C–N bonds are shorter than C–C single bonds and C=C double bonds are present in PET. The presence of the C=O double bond in PA leads to a discernible increase in intensity of the first minimum for $r > 1$ Å in the PA-RDF compared with the PE-PDF. For distances above 5.25 Å, peaks are absent in the PET RDF (Fig. 5a). This value resembles almost the same length as the rigid part of the monomer terephthalic acid (Fig. 5b, PET). Beyond this threshold length, the PET under examination appears to be fully amorphous. This can be rationalized by the free rotation around the C–C single bonds of the ethylene part that allows the monomers to take all possible conformations with respect to each other.

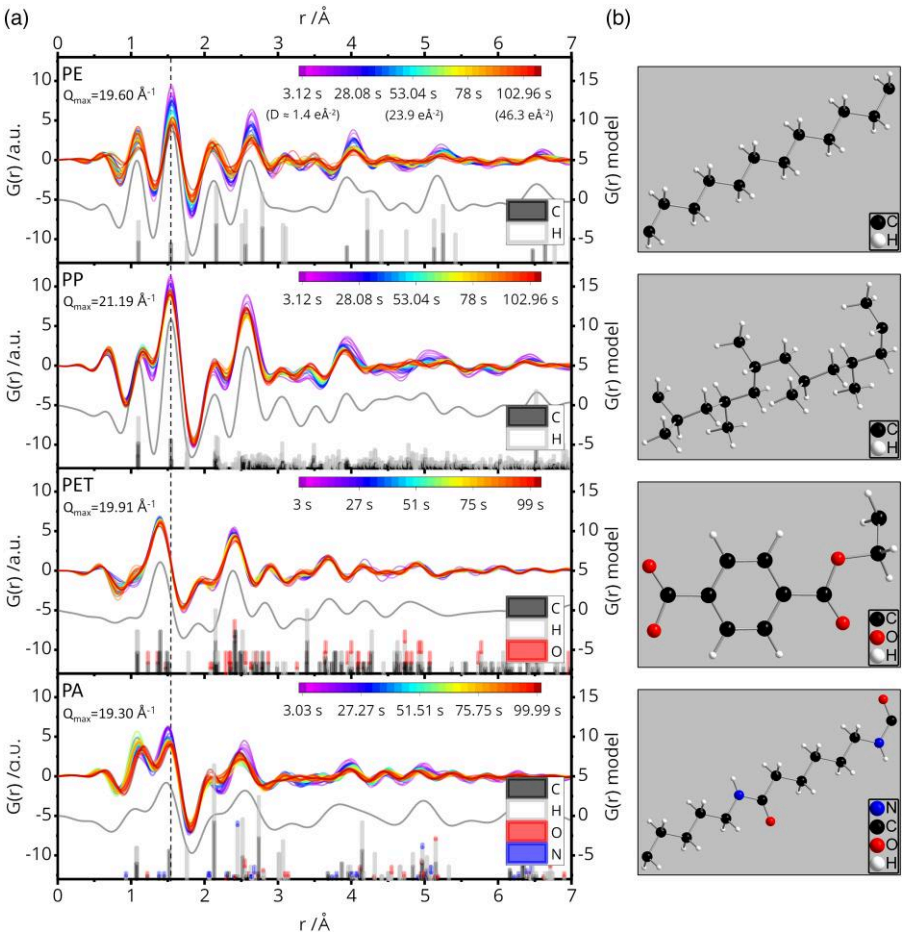

Fig. 5. Comparison of experimental (dose-dependent) and model RDFs determined from the ED time series at a low dose rate of $d_r \cong 0.45$ e Å^{-2} s^{-1}), "TMF-like" conditions. The total applied dose was $D \cong 46$ e Å^{-2}. (**a**) RDFs with the measurement time indicated by the color scale bar, a qualitatively fit model (gray, offset) and the histogram of the r_{jk} employed in the calculation of the model RDF (bar chart, not to scale; the atoms j are the element indicated in the legend). The integration range was $Q_{min} = 2.51$ Å^{-1} for all materials and $Q_{max} = 19.6$ (PE), 21.2 (PP), 19.9 (PET), and 19.3 (PA) Å^{-1}. The dashed line is drawn at the C–C bond length, $r = 1.55$ Å. (**b**) The structural models employed in the calculation of the model RDFs shown in (**a**).

The RDFs of PA show an evolution under the beam influence that is similar to that of PE with the exception of slight shifts of the carbon bonds (C–C, C–N, and C=O), peak at ~1.45 Å and the 2nd neighbor distance peak at ~2.5 Å. Interestingly, this could point to an incidental breaking of carbon–heteroatom bonds instead of C–C bond radiolysis.

Note that the materials under the beam show a complex behavior with regard to morphological changes, which is reflected in the fit factor N (Supplementary Figs. 2–9), as N is proportional to the number of scatterers under the beam and may be influenced by sputtering, melting or drift of the material.

Measurements under Dow-Like Conditions

Analogous to the investigations under TMF-like conditions at $d_r \cong 0.45$ e Å^{-2} s^{-1}, ED patterns at higher dose rates of $d_r \cong 1.6$ e Å^{-2} s^{-1} were recorded. The resulting RDFs are presented in Figure 6. The underlying ED series and a data overview for each series are available in the ESI (Supplementary Videos 5–8 and Figs. 6–9). Under Dow-like conditions, the evolution of the RDFs for all polymers is qualitatively different from the low-dose rate experiments. For PE and PP, it could be interpreted as carbonization of the material with increasing electron dose. We deduce this for the following reasons: first, a decrease of the peak intensity of the C–H bond peaks at $r \cong 1.1$ Å and $r \cong 2.2$ Å, second, an increase of the peak area of the C–C first neighbor distance, and third, a shift of the two C–C peak maxima to shorter distances. These observations can be assigned to the loss of hydrogen, cross-linking of the chains by C–C bond formation, the formation of C–C double bonds, and last ring formation. In the case of PA, the same observation can be made, while here, N–H, N–C, O–H, and O–C peaks are superimposed with the C–H and C–C peaks. It is likely that heteroatoms are present in the resulting graphite-like compound. In contrast, the RDFs of PET show a shift of the two principal peaks to slightly longer distances without significant change in the overall shape of the RDF. Nonetheless, this change could also be attributed to a cleavage of C–H bonds and the formation of (longer) C–C single bonds.

Nanoplastic

If the TEM is to be used in an application to plastics, its field of application will be in detecting the smallest size fractions of particles, i.e., nanoplastics. To assess a lower particle size boundary, we applied the ePDF method to nano-sized plastics, i.e., 100 nm PS (Figs. 7a–7c) spheres. For comparison, 100-nm amorphous silica (a-SiO_2) spheres were chosen representing the environmental inorganic matrix (Figs. 7d–7f).

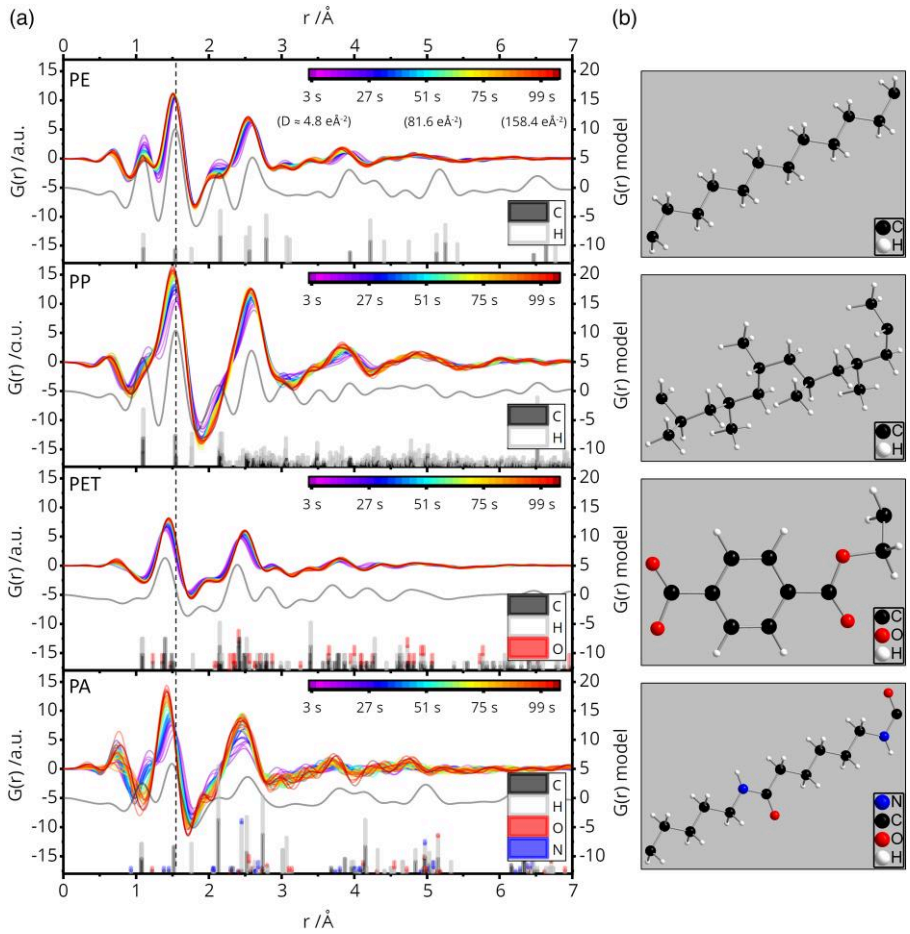

Fig. 6. The structural evolution at moderate electron doses, "Dow-like" conditions. The dose rate was $d_r \cong 1.6$ e Å^{-2} s^{-1} and the total applied dose was $D \cong 160$ e Å^{-2}. (**a**) RDFs for different polymers and exposure time (the plot legend is described in the caption of Fig. 3). The integration range was $Q_{min} = 2.51$ Å^{-1} and $Q_{max} = 21$ Å^{-1} for all materials. The dashed line is drawn at the C–C bond length, $r = 1.55$ Å. (**b**) The structural models employed in the calculation of the model RDFs shown in the left column. The total dose of $D \cong 46$ e Å^{-2} applied under TMF-like conditions (Fig. 3) is reached after 27–30 s of measurement time (blue graphs).

Representative TEM images of the PS and a-SiO_2 spheres are shown in Figures 7a and 7d, respectively. ED (PS, Fig. 7b, and a-SiO_2, Fig. 7e) was recorded using a nanobeam configuration with a beam diameter of 75 nm. As indicated by the shadow images, i.e., the strongly defocused direct beam of the diffraction patterns, which show exactly the material under the beam that contributes to the diffraction pattern. For PS and a-SiO_2 spheres (Figs. 7c, 7f), the ED patterns were recorded on individual particles. As indicated by the experimental RDFs for PS and a-SiO_2 (Fig. 7g), this method is robust enough to extract structural information even from single nanoparticles. Figure 7g further highlights that the resulting RDFs of PS and a-SiO_2 are distinct and in agreement with their expected amorphous configurations and models (PS in Fig. 7h (Natta et al., 1960) and a-SiO_2 in Fig. 7i, alpha-christobalite, ICSD #403365). This shows that the ePDF method can be applied to particles of 100 nm diameter.

Discussion

We have applied a procedure that allows the acquisition of high-quality ED patterns at low electron doses, which are sufficient for RDF analysis up to a momentum transfer of $Q_{max} = 21$ Å^{-1} on beam-sensitive materials. Model RDFs and experimental RDFs, which both include C–H pair distance peaks, are in agreement and allow the distinction of the examined polymers, which was the primary objective of this study.

The relatively high-momentum transfer range Q_{max} is important, because it directly affects the width of peaks in the RDF (Takeshi & Billinge, 2012). A careful, iterative fitting procedure is necessary to reveal the coherently scattered intensity in the ED patterns and to gain RDFs that also show C–H bond intensities. This is achieved by assuming that the first peak in the RDF needs to have an intensity close to that of the correct model. If the assumed stoichiometry is correct, all remaining intensity in the ED is due to incoherent or multiple scattering processes and can be strongly suppressed by subtraction of a polynomial fit (Mu et al., 2013). The "forward and reverse" approach of calculating first the model diffraction pattern and then the model RDF using parameters that match to the parameters of the experimental calculation has several advantages over the alternative histogram-like modeling approach. The "forward and reverse" approach facilitates the direct comparison of the influence of the experimental resolution of ED patterns, the artifacts caused by the moving average filter, the contributions of the fitting error caused by the convolution of the PDF with the atomic scattering factors or deviations in the stoichiometry of the sample, and the Fourier truncation error. The peak widths in the model RDFs are solely a consequence of the choice of Q_{min} and Q_{max}. No

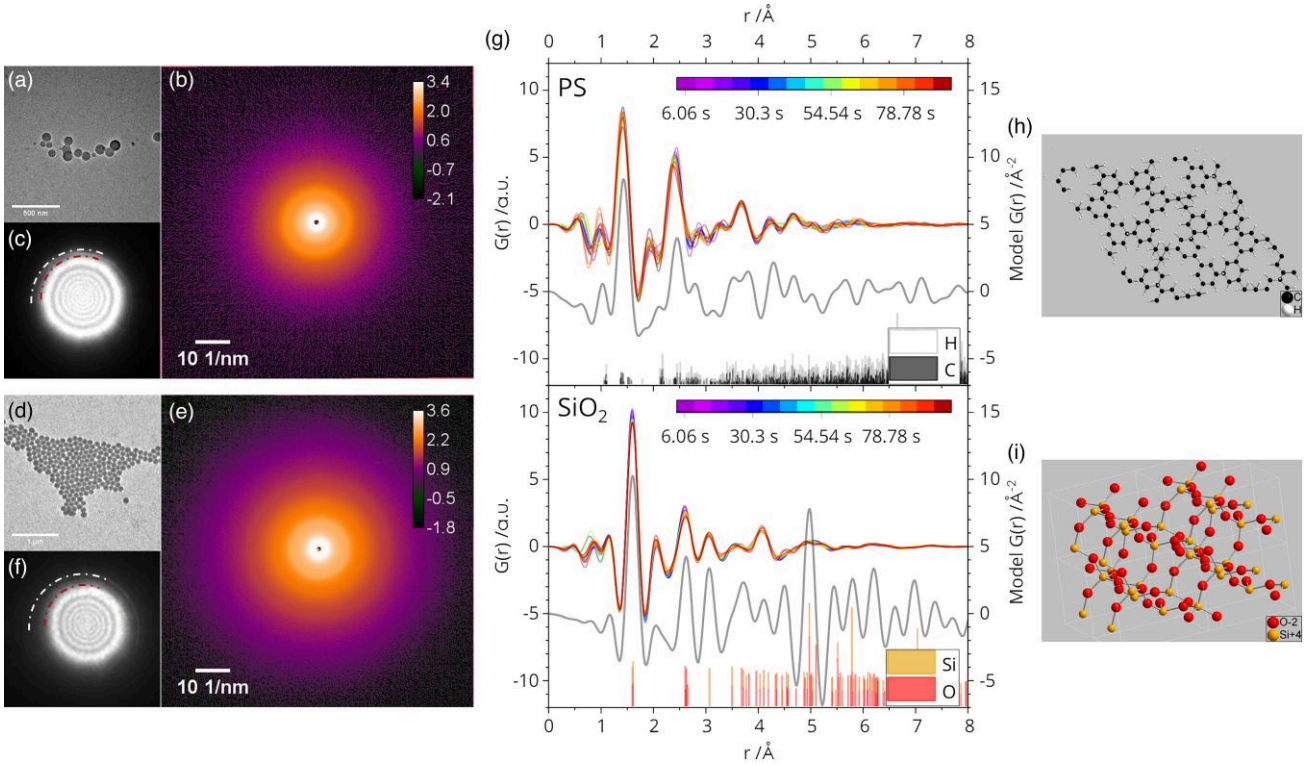

Fig. 7. Comparison of ePDFs of 100-nm–sized PS with 100-nm–sized a-SiO_2 spheres. (**a**) TEM of PS particles after ED measurements. (**b**) First frame of serial ED measured on a PS sphere. (**c**) Shadow image of the beam (diameter ~75 nm, indicated by the red dashed line) on the PS sphere (indicated by the white dashed line). (**d**) TEM of a-SiO_2 particles after ED measurements. (**e**) First frame of serial ED measured on an a-SiO_2 sphere. (**f**) Shadow image of the beam (diameter ~75 nm) on the a-SiO_2 sphere. (**g**) Plots of corresponding RDFs of PS (top) and SiO_2 (bottom). (**h**) Structural model of PS used for the calculation of model $G(r)$ in C (Natta et al., 1960). (**i**) Structural model of SiO_2 used for the calculation of model $G(r)$ in C (alpha-christobalite, ICSD #403365).

assumptions on thermal displacement factors are needed to be made, which is an advantage, if only the local chemical structure, i.e., the conformation independent range of a respective polymer-PDF, is of interest.

As we examined reference materials for microplastic found in the environment, a major problem was the strongly varying thickness of the irregularly shaped particles and their large size with dimensions of the order of 5–200 μm. In most cases, the particles were thin enough for SAED analysis only on their edges and the data presented in this study were recorded on such regions (Supplementary Figs. 2e–9e and 11e). Under low dose conditions, it was often difficult to locate these particle regions. Thus, many measurements had to be discarded as they were too low in quality for RDF calculation because of strong multiple and inelastic scattering caused by thickness effects.

In such a case, the diffuse scattering may obscure the features of the structure function $F(Q)$ and the signal may become dominated by random noise at higher Q values. The structure function then needs to be truncated at a lower Q value for the calculation of the RDF $G(r)$. This results in broad and overlapping peaks in the RDFs, which may prevent a structural identification. Alternatively, if the structure function $F(Q)$ is not truncated at low Q values and the random noise is included in the FT, then, the resulting RDF will contain fast oscillating ripples, which do not give structural information and will obscure the structural peaks.

However, the suitability of the diffraction data for ePDF can be judged in several instances of the derivation, e.g., the scattering of the direct beam in the ED patterns should be low. The fitting result of the factor N should be small. The ratio of features of the uncorrected structure function $F(Q)$ versus the polynomial fit maximum should be large. The signal-to-noise ratio at high Q values should be high. And last, the corrected structure function $F(Q)$ should be in good agreement with the modeled structure function.

Although we achieve a high-real space resolution in the RDFs due to the large Q_{max}, a further improvement of the diffraction data may be possible by the application of energy filtering, especially on thicker particle regions.

While the materials examined in this study are very beam sensitive, a meaningful characterization was possible even without the application of cryo conditions, as the beam dose, dose rate, and irradiation area were reduced to a necessary minimum (TMF-like conditions). The possibility to work without cryo conditions is of advantage, as complications such as ice formation are excluded.

By analyzing a time series of ED, we are able to show the dose dependent structural changes in the materials in the series of RDFs. Those changes are qualitatively different for the two different beam (i.e., TMF-like and Dow-like) conditions that were applied, which is evident in particular in the peak intensities that can be attributed to C–H bonds and C–C bonds. This shows the strength of the ePDF method with regard to the radiation effect and should open the door to its application to more systematic radiolysis studies on materials of interest such as coatings or medical appliances (Gueven, 2004). The effects of radiation on the structure of polymers have been studied previously by X-ray diffraction–based PDF analysis, e.g., PP (Wang & Yeh, 1981) and PE (Chang & LaVerne, 1999).

However, to the best of our knowledge, the direct observation of C–H bond radiolysis in the ePDF series as it is shown in the present study is unprecedented.

As shown in the presented experiments on 100-nm PS spheres (Figs. 7a–7c and 7g) and in previously reported 4D-STEM experiments (Mu et al., 2016, 2019; Wang et al., 2021), the ePDF method can be applied with a spatial resolution on the nanoscale.

Comparing our observations to the most recent study (Kisielowski et al., 2022), we have chosen experimental conditions which can be qualitatively compared with the two sets of experimental conditions described in that article: here called "TMF-like" and "Dow-like." While a minor conclusion of their study is that radiation hardness of HDPE could not be improved by applying ultra–low-dose TMF conditions in comparison with Dow conditions, this was only analyzed with respect to the preservation of Bragg intensities with increasing total dose D. Yet, from our measurements, one can interpret that the loss of intensity of Bragg peaks does not have to go along with severe radiolysis but can be predominantly caused by way of phonon excitation and lattice heating under TMF-like conditions (Fig. 5). Only under "Dow-like" conditions (higher dose rate and larger illuminated area), radiolysis becomes frequent enough to be clearly observed in the ePDF (Fig. 6). As both the phonon and plasmon interactions in the sample increase under the Dow-like conditions, the observed increase in chemical change could be caused by stronger local heating and direct plasmon excitation of the sample at the same time.

Conclusion

The aim of this study was an evaluation of the ePDF method as a characterization method for micro- and nanoplastic. In summary, we have shown that the ePDF method is a powerful tool to gain structural information on beam-sensitive amorphous or semicrystalline organic polymers. Experimental RDFs for the most common polymers in the environment are in good agreement with the structural models even for amorphous 100-nm PS spheres when measured with nanobeam configuration (beam diameter: 75 nm). Our results suggest that a reliable distinction could be made by comparison of the RDFs of PET and either PE, PP, or PA based on the observed intensities in the respective conformation-independent regions. A distinction among the latter may be possible, yet an examination of thickness or vibrational effects on the reliability of the distinction is needed.

Furthermore, the systematic appearance of C–H pair distance peaks in our measurements exemplifies an advantage of the ePDF method over X-ray–based PDF, which usually cannot gain information about hydrogens. We have further extended the ePDF method to the beam dose– and dose rate–dependent domains by recording serial ED. In consequence, electron beam–induced structural changes can be followed by this method. The approach is extendable to 4D STEM methods and if combined with computational techniques, it could become a valuable tool in the quantification of environmental MNP with sizes of a few micrometers down to the nanoscale.

Availability of Data and Materials

The authors have declared that no datasets apply for this piece.

Supplementary Material

To view supplementary material for this article, please visit https://doi.org/10.1093/micmic/ozad087.

Acknowledgments

The authors thank Dr. Korinna Altmann and Dr. Ulrike Braun from the Bundesanstalt für Materialforschung und -prüfung (BAM) for the discussion and provision of the samples and Dr. Xiaoke Mu from the Karlsruhe Institute of Technology for his advice and for providing a Matlab script which was used as the basis for all calculations in this work.

Financial Support

This work was supported by the German Federal Ministry of Education and Research; Project Repräsentative Untersuchungsstrategien für ein integratives Systemverständnis von spezifischen Einträgen von Kunststoffen in die Umwelt (RUSEKU), BMBF grant No. 02WPL1442A.

Conflict of Interest

The authors declare that they have no competing interest.

References

Abu-Sharkh BF (2004). Influence of tacticity on solubility of propene monomer in isotactic and syndiotactic polypropylene. *Polymer (Guildf)* **45**, 6383–6389. 10.1016/j.polymer.2004.06.058

Alimi OS, Farner Budarz J, Hernandez LM & Tufenkji N (2018). Microplastics and nanoplastics in aquatic environments: Aggregation, deposition, and enhanced contaminant transport. *Environ Sci Technol* **52**, 1704–1724. 10.1021/acs.est.7b05559

Bonham RA, Bartell LS & Kohl DA (1959). The molecular structures of n-pentane, n-hexane and n-heptane. *J Am Chem Soc* **81**, 4765–4769. 10.1021/ja01527a002

Chanakian S, Uhl D, Neff D, Drymiotis F, Park J, Petkov V, Zevalkink A & Bux S (2020). Exceptionally high electronic mobility in defect-rich Eu2ZnSb2-: XBix alloys. *J Mater Chem A* **8**, 6004–6012. 10.1039/C9TA14170G

Chang Z & LaVerne JA (1999). Molecular hydrogen production in the radiolysis of high-density polyethylene. *J Phys Chem B* **103**, 8267–8271. 10.1021/jp9921250

Chupas PJ, Chapman KW, Chen H & Grey CP (2009). Application of high-energy X-rays and pair-distribution-function analysis to nanoscale structural studies in catalysis. *Catal Today* **145**, 213–219. 10.1016/j.cattod.2009.03.026

Culbertson CM, Flak AT, Yatskin M, Cheong PHY, Cann DP & Dolgos MR (2020). Neutron total scattering studies of group II titanates (ATiO3, A2+ = Mg, Ca, Sr, Ba). *Sci Rep* **10**, 1–10. 10.1038/s41598-020-60475-8

Debye P (1915). Zerstreuung von Röntgenstrahlen. *Ann Phys* **351**, 809–823. 10.1002/andp.19153510606

Dümichen E, Eisentraut P, Bannick CG, Barthel AK, Senz R & Braun U (2017). Fast identification of microplastics in complex environmental samples by a thermal degradation method. *Chemosphere* **174**, 572–584. 10.1016/j.chemosphere.2017.02.010

Faull M, Zaliznyak LE, & Taylor T & T G (2021). Assessing diversity, abundance, and mass of microplastics (~ 1–300 μm) in aquatic systems. *Limnol Oceanogr Methods* **19**, 369–384.

Geyer R, Jambeck JR & Law KL (2017). Production, use, and fate of all plastics ever made. *Sci Adv* **3**, 19–24. 10.1126/sciadv.1700782

Goedecke C, Dittmann D, Eisentraut P, Wiesner Y, Schartel B, Klack P & Braun U (2020). Evaluation of thermoanalytical methods equipped with evolved gas analysis for the detection of microplastic

in environmental samples. *J Anal Appl Pyrolysis* **152**, 104961. 10.1016/j.jaap.2020.104961

Golmohammadi N, Boland-Hemmat M, Barahmand S & Eslami H (2020). Coarse-grained molecular dynamics simulations of poly(-ethylene terephthalate). *J Chem Phys* **152**, 1–14. 10.1063/1.5145142

Gorelik TE, Neder R, Terban MW, Lee Z, Mu X, Jung C, Jacob T & Kaiser U (2019). Towards quantitative treatment of electron pair distribution function. *Acta Crystallogr Sect B Struct Sci Cryst Eng Mater* **75**, 532–549. 10.1107/S205252061900670X

Gorelik TE, Schmidt MU, Kolb U & Billinge SJL (2015). Total-scattering pair-distribution function of organic material from powder electron diffraction data. *Microsc Microanal* **21**, 459–471. 10.1017/S1431927614014561

Gueven O (2004). An overview of current developments in applied radiation chemistry of polymers. *INTERNATIONAL ATOMIC ENERGY AGENCY, Advances in Radiation Chemistry of Polymers – Proceedings of a technical meeting held in Notre Dame, Indiana, USA 13–17 September 2003, IAEA-TECDOC-1420, IAEA, Vienna (2004)*, 33–39.

Gupta MR & Yeh GSY (1978). DRDF studies of glassy and partially crystalline poly(ethylene terephthalate). *J Macromol Sci Part B* **15**, 119–137. 10.1080/00222347808212249

Gupta M & Yeh GSY (1979). Application of paracrystalline lattice theory to the analysis of differential radial distribution function of amorphotized polyethylene. *J Macromol Sci Part B* **16**, 225–241. 10.1080/00222347908212293

Hilderbrandt RL & Bonham RA (1971). Structure determination by gas electron diffraction. *Annu Rev Phys Chem* **22**, 279–312. 10.1146/annurev.pc.22.100171.001431

Hoque MM, Vergara S, Das PP, Ugarte D, Santiago U, Kumara C, Whetten RL, Dass A & Ponce A (2019). Structural analysis of ligand-protected smaller metallic nanocrystals by atomic pair distribution function under precession electron diffraction. *J Phys Chem C* **123**, 19894–19902. 10.1021/acs.jpcc.9b02901

Huan TD, Mannodi-Kanakkithodi A, Kim C, Sharma V, Pilania G & Ramprasad R (2016). A polymer dataset for accelerated property prediction and design. *Sci Data* **3**, 1–10. 10.1038/sdata.2016.12

Kavesh S & Schultz JM (1970). Lamellar and interlamellar structure in melt-crystallized polyethylene. I. Degree of crystallinity, atomic positions, particle size, and lattice disorder of the first and second kinds. *J Polym Sci Part A-2: Polym Phys* **8**, 243–276. 10.1002/pol.1970.160080205

Kisielowski C, Specht P, Rozeveld S, Freitag B, Kieft ER, Kang J, Fielitz AJ, Fielitz TR, van Dyck D & Yancey DF (2022). Exploring functional materials by understanding beam-sample interactions. *Adv Funct Mater* **32**, 2201112. 10.1002/adfm.202201112

Kisielowski C, Specht P, Rozeveld SJ, Kang J, Fielitz AJ, Barton D, Salazar AC, Dubon OD, Van Dyck D & Yancey DF (2021). Modulating electron beam-sample interactions in imaging and diffraction modes by dose fractionation with low dose rates. *Microsc Microanal* **27**, 1420–1430. 10.1017/S143192762101268X

Kobryn AE, Nikolić D, Lyubimova O, Gusarov S & Kovalenko A (2014). Dissipative particle dynamics with an effective pair potential from integral equation theory of molecular liquids. *J Phys Chem B* **118**, 12034–12049. 10.1021/jp503981p

Koelmans AA, Mohamed Nor NH, Hermsen E, Kooi M, Mintenig SM & De France J (2019). Microplastics in freshwaters and drinking water: Critical review and assessment of data quality. *Water Res* **155**, 410–422. 10.1016/j.watres.2019.02.054

Kögel T, Bjorøy Ø, Toto B, Bienfait AM & Sanden M (2020). Micro- and nanoplastic toxicity on aquatic life: Determining factors. *Sci Total Environ* **709**, 136050. 10.1016/j.scitotenv.2019.136050

Kübel C, González-Ronda L, Drummy LF & Martin DC (2000). Defect-mediated curvature and twisting in polymer crystals. Journal of Physical Organic Chemistry **13**, 816–829. 10.1002/1099-1395(200012)13:12%3C816::AID-POC322%3E3.0.CO;2-I

Kumar S & Adams WW (1990). Electron beam damage in high temperature polymers. *Polymer (Guildf)* **31**, 15–19. 10.1016/0032-3861(90)90341-U

Laridjani M & Leboucher P (2009). The structural dilemma of bulk polyethylene: An intermediary structure. *PLoS ONE* **4**, e6228. 10.1371/journal.pone.0006228

Lobato I & Van Dyck D (2014). An accurate parameterization for scattering factors, electron densities and electrostatic potentials for neutral atoms that obey all physical constraints. *Acta Crystallogr Sect A Found Adv* **70**, 636–649.

Marigo A, Marega C, Zanetti E, Zannetti R & Paganetto G (1991). X-ray diffraction characterization of amorphous poly(propylene). *Macromol Chem Phys* **192**, 523–529. 10.1002/macp.1991.021920305

Mintenig SM, Bäuerlein PS, Koelmans AA, Dekker SC & Van Wezel AP (2018). Closing the gap between small and smaller: Towards a framework to analyse nano- and microplastics in aqueous environmental samples. *Environ Sci Nano* **5**, 1640–1649.

Mu X, Mazilkin A, Sprau C, Colsmann A & Kübel C (2019). Mapping structure and morphology of amorphous organic thin films by 4D-STEM pair distribution function analysis. *Microscopy* **68**, 301–309. 10.1093/jmicro/dfz015

Mu X, Neelamraju S, Sigle W, Koch CT, Totò N, Schön JC, Bach A, Fischer D, Jansen M & Van Aken PA (2013). Evolution of order in amorphous-to-crystalline phase transformation of MgF2. *J Appl Crystallogr* **46**, 1105–1116. 10.1107/S0021889813011345

Mu X, Wang D, Feng T & Kübel C (2016). Radial distribution function imaging by STEM diffraction: Phase mapping and analysis of heterogeneous nanostructured glasses. *Ultramicroscopy* **168**, 1–6. 10.1016/j.ultramic.2016.05.009

Narten AH (1989). Radial distribution of carbon atoms in crystalline and molten polyethylene from x-ray diffraction. *J Chem Phys* **90**, 5857–5860. 10.1063/1.456391

Natta G, Corradini P & Bassi IW (1960). Crystal structure of isotactic polystyrene. *Il Nuovo Cimento* **15**, 68–82. 10.1007/BF02731861

Neissendorfer F (1982). Investigation of short range ordering in poly(-ethylenen terephthalate) by means of differential radial distribution function. *Acta Polym* **33**, 395–396. 10.1002/actp.1982.010330616

Ng E, Huerta E, Eldridge SM, Johnston P, Hu H, Geissen V & Chen D (2018). Science of the total environment an overview of microplastic and nanoplastic pollution in agroecosystems. *Sci Total Environ* **627**, 1377–1388. 10.1016/j.scitotenv.2018.01.341

Nguyen B, Claveau-Mallet D, Hernandez LM, Xu EG, Farner JM & Tufenkji N (2019). Separation and analysis of microplastics and nanoplastics in Complex environmental samples. *Acc Chem Res* **52**, 858–866. 10.1021/acs.accounts.8b00602

Paul A, Wander L, Becker R, Goedecke C & Braun U (2019). High-throughput NIR spectroscopic (NIRS) detection of microplastics in soil. *Environ Sci Pollut Res* **26**, 7364–7374. 10.1007/s11356-018-2180-2

Petkov V, Ren Y, Kabekkodu S & Murphy D (2013). Atomic pair distribution functions analysis of disordered low-Z materials. *Phys Chem Chem Phys* **15**, 8544–8554. 10.1039/c2cp43378h

Primpke S, Christiansen SH, Cowger W, De Frond H, Deshpande A, Fischer M, Holland EB, Meyns M, O'Donnell BA, Ossmann BE, Pittroff M, Sarau G, Scholz-Böttcher BM & Wiggin KJ (2020). Critical assessment of analytical methods for the harmonized and cost-efficient analysis of microplastics. *Appl Spectrosc* **74**, 1012–1047. 10.1177/0003702820921465

Proffen T, Billinge SJL, Egami T & Louca D (2003). Structural analysis of complex materials using the atomic pair distribution function—A practical guide. *Zeitschr Kristallogr* **218**, 132–143.

Reimer L (1984). Methods of detection of radiation damage in electron microscopy. *Ultramicroscopy* **14**, 291–303. 10.1016/0304-3991(84)90097-4

Sheng HW, Luo WK, Alamgir FM, Bai JM & Ma E (2006). Atomic packing and short-to-medium-range order in metallic glasses. *Nature* **439**, 419–425. 10.1038/nature04421

Simon P & Argay G (1978). Revised atomic coordinates of crystalline nylon-6. *J Polym Sci Polym Phys Ed* **16**, 935–937.

Takeshi E & Billinge SJL (2012). The method of total scattering and atomic pair distribution function analysis. *Pergamon Mater Ser* **16**, 55–111. 10.1016/B978-0-08-097133-9.00003-4

Terban MW, Pütz AM, Savasci G, Heinemeyer U, Hinrichsen B, Desbois P & Dinnebier RE (2020). Improving the picture of atomic structure in nonoriented polymer domains using the pair distribution function: A study of polyamide 6. *J Polym Sci A* **58**, 1843–1866. 10.1002/pol.20190272

Wander L, Vianello A, Vollertsen J, Westad F, Braun U & Paul A (2020). Exploratory analysis of hyperspectral FTIR data obtained from environmental microplastics samples. *Anal Methods* **12**, 781–791. 10.1039/C9AY02483B

Wang K, Hua W, Li Z, Wang Q, Kübel C & Mu X (2021). New insight into desodiation/sodiation mechanism of MoS2: Sodium insertion in amorphous Mo–S clusters. *ACS Appl Mater Interfaces* **13**, 40481–-40488. 10.1021/acsami.1c07743

Wang CS & Yeh GSY (1981). Effects of radiation on the structure of polypropylene. *Polym J* **13**, 741–747. 10.1295/polymj.13.741

Wecker SM, Davidson T & Cohen JB (1972). A structural study of glassy polystyrene. *J Mater Sci* **7**, 1249–1259. 10.1007/BF00550690

Willinger E, Massué C, Schlögl R & Willinger M-G (2017). Identifying key structural features of IrOx water splitting catalysts. *J Am Chem Soc* **139**, 12093–12101. 10.1021/jacs.7b07079

Zhabanov YA, Zakharov AV, Giricheva NI, Shlykov SA, Koifman OI & Girichev GV (2015). To the limit of gas-phase electron diffraction: Molecular structure of magnesium octa(m-trifluoromethylphenyl) porphyrazine. *J Mol Struct* **1092**, 104–112. 10.1016/j.molstruc.2015.03.010